Dedicated to Shinya Inoué, Distinguished Scientist at the Marine Biological Laboratory

Analysis of edge birefringence

Rudolf Oldenbourg
Marine Biological Laboratory, Woods Hole, Massachusetts 02543 and Martin Fisher School of Physics, Brandeis University, Waltham, Massachusetts 02254 USA

ABSTRACT We present an experimental and theoretical study of the phenomenon of edge birefringence that appears near boundaries of transparent objects which are observed with high extinction and high resolution polarized light microscopy. As test objects, thin flakes of isotropic KCl crystals were immersed in media of various refractive indices. The measured retardation near crystal edges increased linearly with both the crystal thickness (tested between 0.3 and 1 μm), and the difference in refractive indices n between crystal ($n = 1.49$) and immersion liquids (n between 1.36 and 1.62). The specific edge birefringence, i.e., the retardation per thickness and per refractive index difference, is 0.029 on the high refractive index side of the boundary and −0.015 on the low refractive index side. The transition through zero birefringence specifies the position of a boundary at a much higher precision than predicted by the diffraction limit of the optical setup. The theoretical study employs a ray tracing procedure modeling the change in phase and polarization of rays passing through the specimen. We find good agreement between the model calculations and the experimental results indicating that edge birefringence can be attributed to the change in polarization of light that is refracted and reflected by dielectric interfaces.

INTRODUCTION

The polarizing microscope has traditionally been an important tool for studying mineral composition, determining optical parameters of crystals, and for analyzing fine structure in fibers, etc. (Hartshorne and Stuart, 1960). Ambronn and Frey (1926) and Schmidt (1924, 1937) pioneered the application of polarized light microscopy to biological objects, and Inoué and co-workers explored its use for the study of fine structure directly in living cells (Inoué and Dan, 1951; Inoué, 1953; Inoué and Sato, 1966).

During these applications of polarized light microscopy in biology, it became increasingly desirable to detect and measure ever smaller magnitudes of birefringence retardation, and to resolve ever finer specimen detail. In classical polarization microscopy, the high extinction needed for detecting weak retardations was incompatible with the large numerical aperture (NA) of the lenses needed for high resolution owing to the depolarization of light by differential loss of the components polarized parallel and perpendicular to the plane of incidence at the high NA optical interfaces (Wright, 1911). This limitation was overcome with the introduction of the polarization rectifier (Inoué and Hyde, 1957), which also eliminated the diffraction anomaly that is observed in nonrectified polarizing microscopes (Inoué and Kubota, 1958).

As higher extinction could be attained simultaneously with greater image resolution, however, what appeared to be a thin birefringent layer became evident at the edges or boundaries of many objects (Inoué, 1959). On the higher refractive index side of the boundary, the slow axis of the birefringent layer lay parallel to the interface and on the lower index side the slow axis lay perpendicular to the interface. The "edge birefringence" (unlike intrinsic birefringence due to the intrinsic anisotropy of oriented molecules) seemed to disappear when the refractive index gradient at the boundary was abolished, and (unlike form birefringence due to the alignment of submicroscopic rodlets or platelets) reappeared with the slow axis directions turned by 90° when the refractive index of the medium was raised above or below that of the object.

Edge birefringence appears at all specimen boundaries where there exists a sharp gradient or discontinuity of refractive index regardless of the material phase on the two sides of the boundary, solid-liquid, solid-gas, liquid-liquid, liquid-gas, etc. Despite its general nature, edge birefringence has eluded a clear physical explanation and a thorough experimental study, that would allow quantification of its impact on the image formation in the polarizing microscope. Inoué and Szent-Gyorgyi (1958), for example, saw edge birefringence at optical boundaries in isolated muscle fibrils, flanking the Z- and H-bands, at the A- and I-band boundaries, etc., but mistook these "birefringent bands" to reflect real anisotropic structures. Such an interpretation was all the more tempting because these bands changed their retardance and relative positions during ATP-induced shortening of the myofibrils and upon extraction of their component proteins (S. Inoué, personal communication).

0006-3495/91/09/629/13 $2.00

With the advent of high extinction video microscopy and digital image processing, the light microscope can now be used for resolving extremely fine specimen detail as well as for visualizing thin objects with minute phase difference or birefringence retardation. Thus one can even display the motility and polymerization–depolymerization behavior of unresolved objects such as the 25-nm diam microtubules (Walker et al., 1989); and the three-dimensional geometry of an even thinner, single bacterial flagellum (Block et al., 1991).

As the power of light microscopes employing polarized light has thus improved, it became increasingly urgent that we understand the nature of optical events taking place at the boundaries of minute structures. That was necessary both to avoid misinterpreting the image and to gain further insight into the specimen fine structure.

In this paper, we report our studies on a model system, (thin flakes of an isotropic crystal, KCl, immersed in media of various refractive indices) on which we measured the magnitude and distribution of edge birefringence as functions of the refractive index of the immersion media, thickness of the crystal and numerical aperture of the illuminating condenser lens.

This is followed by a theoretical analysis of edge birefringence, which takes into account the Fresnel coefficients for the parallel and perpendicular components of the rays reflected by, and passing through, the crystal boundary, and the interference of the ray components at the image plane.

As demonstrated, results of the theoretical calculations agree well with our measurements made with the aid of high extinction video microscopy on the model specimens. Our theoretical results give us a basic understanding of the optical processes contributing to the edge birefringence phenomenon and our experimental results provide the first detailed and quantitative account of edge birefringence and its influence on the image formation in the polarizing microscope. In the last section we will discuss the implications of these findings.

MATERIALS AND METHODS

Sample preparation

Small KCl crystals were prepared by squirting a drop of saturated KCl solution into ~1 ml ethanol. Immediately, a white precipitate formed, consisting of small crystals typically of <10 μm diam (Fig. 1). A small sample of the precipitate in ethanol was transferred to a microscope slide, covered with a coverslip and sealed with Valap-B (a 1:1:1 simmered mixture of vaselline, lanolin, and bee's wax). Slides and coverslips were selected for low stress birefringence. Most crystals were cubic in shape, although a few formed as thin flakes. We selected these thin isotropic crystal flakes as our test objects.

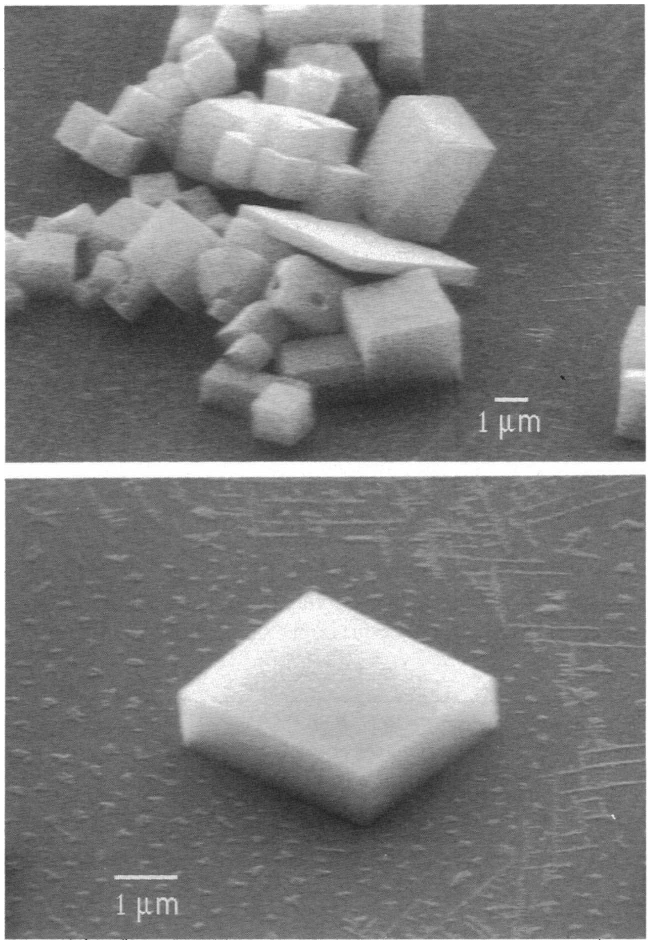

FIGURE 1 KCl crystals in scanning electron microscope (SEM). The crystals were formed in the precipitate when a drop of saturated KCl solution was squirted into ethanol. Part of the precipitate was transferred with a Pasteur pipette to the SEM substrate. The ethanol was evaporated in the vacuum chamber and the crystals covered with a metal coating of ~200-Å thickness.

For the imbibition measurements, the coverslip sat on spacers and the assembly remained unsealed. We chose spacers of different thicknesses, so that the coverslip was slightly higher on one side (see Fig. 2). The progressively narrower wedge shaped space forces the perfusion fluid to spread and more reliably imbibe the specimen than with chambers whose height is constant (Lutz and Inoué, 1986). New solvent was applied at the taller side and the solvent was pulled into the wedge-shaped perfusion chamber by capillary forces. At the same time filter paper applied to the low end of the chamber removed excess solvent and kept the chamber flushing during solvent changes.

A small platform, cut from cover glass, was introduced into the middle of the chamber and crystals deposited upon it. The platform reduced the distance between crystals and coverslip to allow the use of oil immersion objectives with high numerical aperture, good optical correction, and small working distance (Inoué, 1990; Keller, 1990). The platform could also be separated from the assembly and transferred to a scanning electron microscope to examine the dimensions of the crystals.

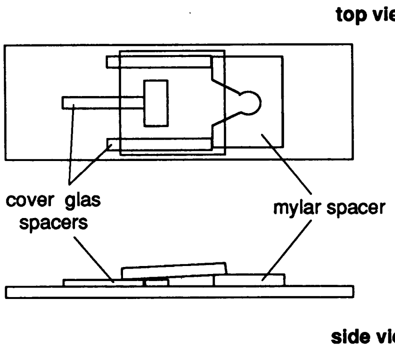

FIGURE 2 Perfusion chamber assembled with a microscope slide, coverslip and spacers. Spacers were cut from no. 1½ cover glass (0.17 mm thick) and mylar (0.28 mm thick). The mylar spacer had a central hole with an angled opening towards the coverslip. In the middle of the chamber, a small piece of cover glass (2 × 4 mm) was placed as a platform for the crystals to be examined. The platform was kept in place by a fourth strip of cover glass spacer. First, all the spacers and the platform were assembled on the slide, then wetted with ethanol. After the ethanl evaporated, the spacers adhered to the slide surface enough to make the assembly mechanically stable for the transfer of the KCl precipitate and placing of the top coverslip.

Light microscopy and digital image processing

KCl crystals were observed in a polarized light microscope equipped with a 100-W mercury arc lamp as light source. The green light of the 546 nm wavelength spectral line was selected with a high transmission interference filter. As microscope stands we used either the universal microscope designed by Inoué and co-workers (Inoué, 1986) or a modified Leitz Ortholux POL microscope. In both microscopes we used rectified oil immersion optics with a maximum numerical aperture (NA) of 1.35 for the condenser and a 100× objective (NA = 1.25), both from Nikon. The separate rectification in condenser and objective increases the extinction for crossed polarizer and analyzer by counteracting the slight rotation of the polarization direction when light is refracted at the curved lens surfaces (Inoué and Hyde, 1957). The high extinction factor of rectified optics increases the contrast between background and birefringent objects and renders faint birefringent features visible. Rectified optics also removes a diffraction anomaly observed in regular polarized light microscopes with high numerical aperture lenses (Inoué and Kubota, 1958).

The rectified objective lens includes a half-wave plate that modifies the polarization state of the light passing through it. For linearly polarized light, the half-wave plate flips the polarization axis with respect to the axis of the wave plate. For ellipitcally polarized light, the half-wave plate not only flips the orientation of the main axes with respect to the plate axis but also inverts the sense of rotation of the ellipitcally polarized light vector. This latter effect changes the sign, but not the magnitude, of retardation of the light passing through the plate, apparently inverting the sign of the specimen birefringence as measured with the compensator. We report our measurements of specimen birefringence as if the half-wave plate were removed and no inversion of the sign had occurred.

Images of crystals were recorded with a Newvicon video camera (Hamamatsu Corp., Middlesex, NJ; C2400) or a video tube camera with SIT intensifier (Daje-MTI Inc., Michigan City, IN; model 65), mounted on the photo tube of the microscope. Video images were captured with a PC-based digital image processing system (Universal Imaging Corp., West Chester, PA; Image1/AT) and averaged over 64 frames. A captured image was stored in the computer memory as a two-dimensional array of integer values between 0 (black) and 255 (white). Integer values were linearly proportional to the light intensity on the camera faceplate for images recorded with the SIT camera (see legend to Fig. 6). The Newvicon camera showed saturation at high light intensities. The dimensions of one picture element or pixel in a digitized video image, expressed in object dimensions, were measured by replacing the sample with a micrometer scale.

Image arrays were transferred to a Macintosh IIx personal computer for further analysis. On the Macintosh, two software programs were used, Image v1.22–1.32 (Wayne Rasband, National Institutes of Health), a public domain image analysis software, and Mathematica (Wolfram Research Inc., Champaign, IL), a system for doing mathematics by computer. The final data analysis, plotting, and model calculations presented here were done with Mathematica.

The thickness of KCl crystals suspended in ethanol was measured with an interference microscope using transmitted light. The interference set, according to Jamin-Lebedeff, is an accessory to the Standard Microscope WL POL from Zeiss. With this microscope, the optical path difference between a reference beam through the solvent and a measuring beam through the crystal was determined. Because the refractive index of both solvent and crystal is known, the thickness of the crystal could be calculated directly from the measured optical path difference. Measurements were taken with the 100/1.0 oil immersion objective. We measured the thickness of the same crystals that were observed with the polarized light microscope. This was achieved by marking the cover slip on the outside surface with a small dot from a felt pen and measuring its position with the translation stage of the microscope. Crystal positions could than be referenced to the same dot and were easily reproduced in both microscopes.

To measure the path difference, crystals were observed in the interference microscope with monochromatic light, the smallest possible condenser and field aperture and a λ/4 plate before the analyzer (Sénarmont compensation). The background appeared darkest when the analyzer was in the crossed position, while the crystal appeared bright. Turning the analyzer in one direction lit up the background and darkened the crystal. When the analyzer was turned by an angle ϕ, the background and crystal appeared equally bright. By turning the analyzer farther, the extinction position of the crystal was reached. In the extinction position, the intensity of the crystal is minimal, while the surrounding solvent is bright. The extinction position is difficult to judge properly by eye. Equal brightness of crystal and solvent, however, can be determined very accurately with the eye. It is easy to show that the angle for extinction is just twice the angle ϕ for equal brightness (Barer, 1959). The thickness d of the crystal is related to the angle 2ϕ (in degree) by

$$d = \frac{2\phi\lambda}{180(n_{\mathrm{KCl}} - n_{\mathrm{ethanol}})},$$

with λ the wavelength of light (546 nm) and n_{KCl} (1.490) and n_{ethanol} (1.361) the refractive index of the crystal and the solvent, respectively.

RESULTS

Intensities and retardance near crystal edges

Fig. 3 shows a typical image of a thin KCl crystal in ethanol viewed in a polarized light microscope. The crystals were recognized by their bright edges against the

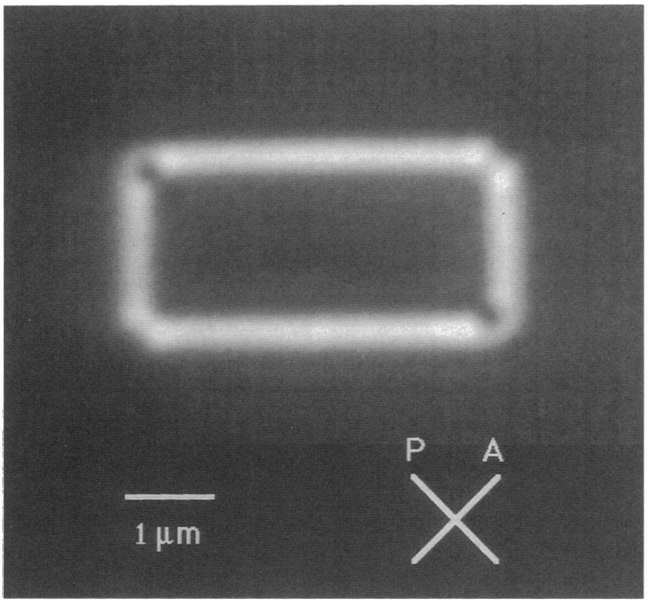

FIGURE 3 Image of thin KCl crystal (0.83 μm thick) in ethanol observed between crossed polarizers in a light microscope equipped with a rectified oil immersion objective (100×, NA 1.25) and condenser (condenser aperture filled to NA 0.6). A 1-μm scale bar and the orientations of polarizer and analyzer are indicated.

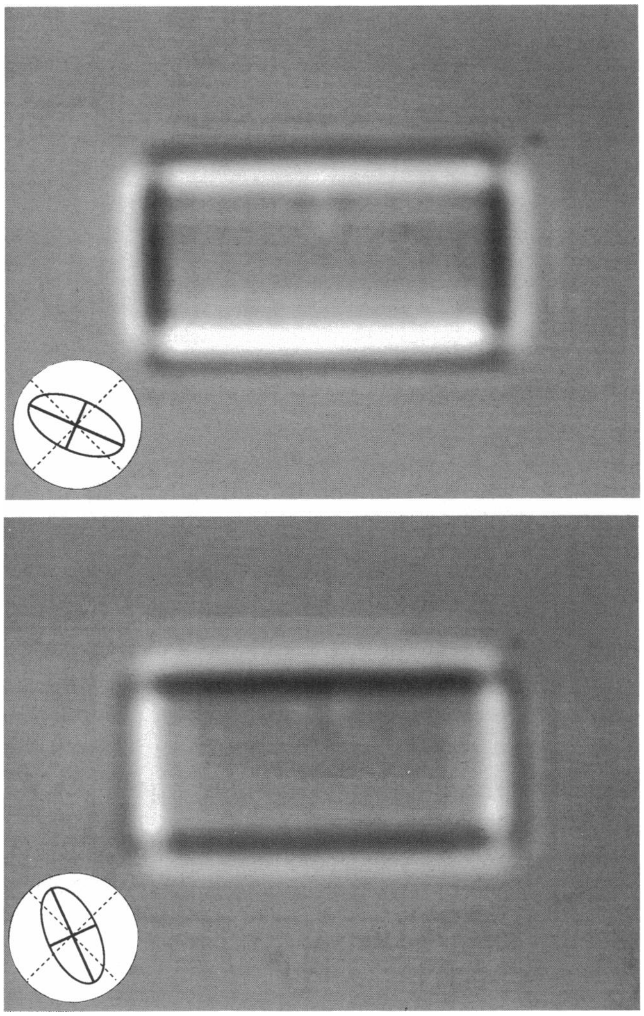

FIGURE 4 The same crystal as in Fig. 3 observed with crossed polarizer and analyzer and an additional thin mica plate (Brace-Köhler compensator, 18.5 nm retardance). The insets illustrate that in the top image the slow axis of the compensator was rotated closer to the horizontal direction (positive rotation angles), whereas in the bottom image it was rotated closer to the vertical direction (negative rotation angles). Each crystal edge is bordered by one intensity minimum and maximum which exchange position when the compensator is rotated from a negative to a positive angle with respect to the extinction position.

dark viewing field of the microscope when the polarizer and analyzer were crossed. The edges were brightest when they were aligned at 45° with respect to the polarizer and analyzer axes. The edges essentially disappeared when they were oriented parallel to the polarizer and analyzer axes. All data presented here were collected with the edges in the 45° position.

Next we added a Brace-Köhler compensator to the imaging path of the microscope with crossed polarizer and analyzer. When we rotated the compensator out of the extinction position by a few degrees, we observed thin layers inside and outside the crystal edges that appeared brighter or darker than the background (Fig. 4). From our observations we derived that the thin layer on the inside of a crystal edge had an apparent positive birefringence (slow axis parallel to the edge), whereas the thin layer on the outside (the solvent side) of the crystal edge had an apparent negative birefringence (slow axis perpendicular to the edge).

To measure the retardation of light arriving at different image points, we recorded images at various compensator settings and obtained intensity scans, similar to the ones in Fig. 5. At small compensator settings image intensities varied as the square of the compensator angle. Fig. 6 demonstrates the good fit of parabolas to the measured intensities versus compensator angles (when larger angles were included in the measurement, the well-known sinusoidal variation of the image intensity was observed). Parabolas fitted to intensities near a crystal edge were displaced to the left or right from the parabola fitted to background intensities. The lateral displacement $\Delta\theta$ of the minimum of a parabola fitted to the data recorded at a given image point is a measure of the retardance R of the light focused at that image point:

$$R = R_0 \sin(2\Delta\theta),$$

with R_0 the retardance associated with the compensator

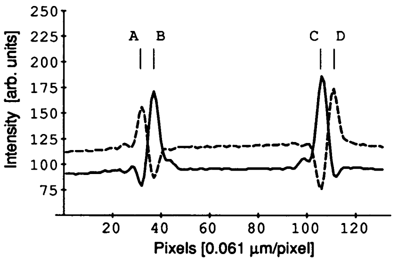

FIGURE 5 Horizontal intensity scans across the vertical crystal edges shown in Fig. 4. The dashed line represents intensity values from the top image (compensator setting +21°), the continuous line represents intensities from the bottom image (compensator −19°). Each scan is the average of 20 horizontal image rows located near the center of the crystal. Vertical lines *A–D* indicate the positions of minima and maxima close to the crystal edges. Distances *A–B* and *C–D* are each six pixels or 0.37 µm wide.

(R_0 = 18.5 nm). For example, the parabolas fitted to intensity data shown in Fig. 6 are displaced laterally by 5.6° (*B*,*C*) and −2.4° (*A*,*D*). Hence, light focused at these image points has a retardance of +3.5 nm (*B*,*C*) and −1.6 nm (*A*,*D*). Positive retardance indicates a phase lag of light polarized parallel to the edge with respect to light polarized perpendicular to the edge, whereas negative retardance results from a phase advance of the light polarized parallel to the edge with respect to perpendicular to the edge.

Each image point has a characteristic retardance which can be computed with the procedure described in the preceding paragraph. Fig. 7 shows the retardance of image points which correspond to the intensity scans of Fig. 5.

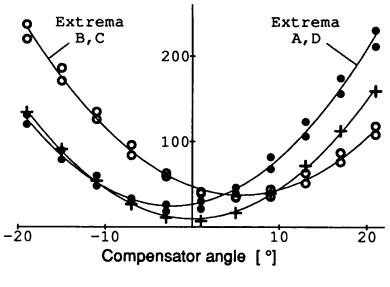

FIGURE 6 Intensities in extrema near crystal edges versus compensator angle. Filled circles are intensities measured in the extrema *A* and *D* outside the crystal, open circles in extrema *B* and *C* inside the crystal (see Fig. 5). Crosses are background intensities taken from the far left end of the intensity scans. Parabolas (*solid lines*) were fitted to each data set. The good fit to the background data indicates a linear relationship between light intensities on the camera faceplate (SIT camera) and corresponding integer values resulting from the image capture procedure.

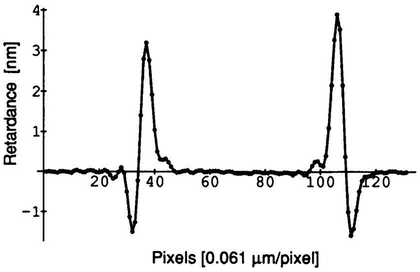

FIGURE 7 Retardances across vertical crystal edges seen in Fig. 4. The retardance values of image points were computed using a set of 11 images recorded at different compensator angles and using the procedure described in the text.

Retardance versus condenser NA and focus position

The retardance measured near a crystal edge depended on both the focus position of the crystal and the numerical aperture (NA) of the condenser. Fig. 8 shows

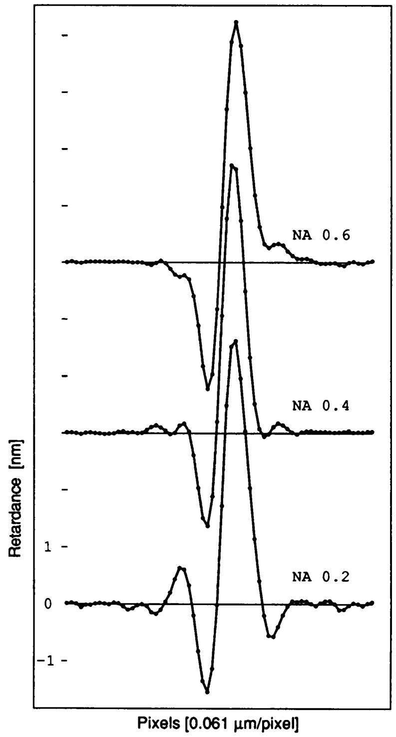

FIGURE 8 Retardance values near a single crystal edge at different settings of the condenser NA (data sets for NA 0.4 and NA 0.6 are displaced vertically, retardance values to the far left and right are near zero for all three data sets). The crystal is 1.0 µm thick and immersed in ethanol. The edge is located between the strong minimum and maximum, near where the retardance goes through zero. The crystal is on the right side, the solvent on the left side of the edge.

retardance values near one crystal edge at different settings of the condenser NA. The figure illustrates the following observations. The positions of the main minimum and maximum of retardance nearest to the edge don't depend on the condenser NA, while their amplitudes increase somewhat with decreasing NA. More dramatically, additional maxima and minima further away from the edge become stronger and shift position, when the condenser NA is reduced. These additional oscillations at low NA appeared to be a diffraction pattern produced by the edge, as discussed later in this article.

The visibility or relative amplitude of the additional extrama further away from the edge depended also on the focus position of the crystal along the optical axis of the microscope. When the crystal was moved in either direction along the microscope axis, starting from the central focus position, the two strong extrema near the edge decreased in amplitude while the additional extrema further away first increased in amplitude and then decreased. For a condenser NA = 0.6, all features reminiscent of the edge became invisible when the crystal was moved to about three times its thickness away from the central focus position. In the following sections we report on the retardance, measured in the extrema near the edge, versus solvent refractive index and crystal thickness. Images for these studies were taken with the crystal in the central focus position and a condenser NA of 0.6.

Retardance versus solvent refractive index

Our microscope perfusion chamber (see Materials and Methods) allowed immersion of the crystals into noninteractive imbibition media with various refractive indices. Immersion of the crystals ($n = 1.490$) in a solvent mixed from 33 vol % ehtanol ($n = 1.361$) and 67 vol % benzylalcohol ($n = 1.532$) rendered the crystals invisible in the microscope, because the refractive indices of solvent and crystals were nearly identical. Flushing the chamber subsequently with pure benzylalcohol, which has a higher refractive index than KCl, made the crystals reappear with reversed contrast. The crystal edges were now decorated with a positive birefringent layer on the solvent side and a negative birefringent layer on the crystal side. A series of imbibition measurements with the same crystal revealed that the amount of retardance on each side of the crystal varied linearly with the absolute value of the difference in refractive index between solvent and crystal (Fig. 9). Solvents used for the imbibition measurements, other than ethanol and benzyalcohol, were nitrobenzene ($n = 1.553$), iodobenzene ($n = 1.622$), and mixtures thereof.

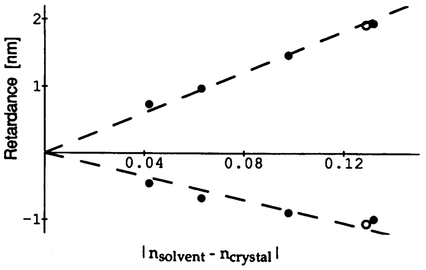

FIGURE 9 Measured retardances near the crystal edge versus the difference in refractive index between the solvent and the KCl crystal (0.52 μm thick). Positive retardances (slow axis parallel to edge) were measured on the high refractive index side, negative retardances (slow axis perpendicular to edge) were measured on the low refractive index side of the crystal edge. Open circles were measured with low refractive index solvent (ethanol), filled circles with solvents having a higher refrative index than the crystal (see text). The slopes of the linear fits, indicated by the dashed lines, are +15.2 and −8.7 nm.

Retardance versus crystal thickness

We have measured the edge birefringence of crystals with different thickness. The thickness of crystals immersed in ethanol was measured with an interference microscope using transmitted light (see Materials and Methods). We found a linear relationship between crystal thickness and measured retardance (Fig. 10).

THEORY AND MODEL CALCULATION

Introduction

The model calculation of the image intensities near a crystal edge was based on a ray tracing procedure which calculated not only the path of a ray but also its phase and state of polarization. The interaction of rays with the crystal surfaces was modeled with Fresnel's equations for the transmission and reflection of light rays falling on a dielectric interface (Hecht, 1987). Fresnel's

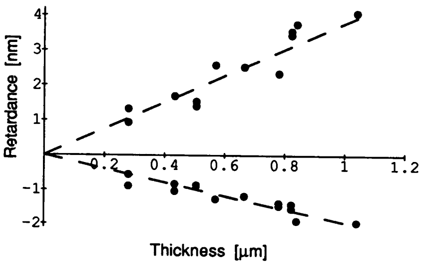

FIGURE 10 Measured retardances near crystal edge versus crystal thickness. Crystals were immersed in ethanol. The slopes of the linear fits, shown by the dashed lines, is +3.8 and −2.0 nm/μm.

equations describe the phase shift and the change in amplitude of rays that are transmitted through and reflected by the interface. In Fig. 11 a graphical representation is given of the amount of phase shift introduced by the reflection of rays impinging on the interface at different angles of incidence. The amplitude of reflected rays is only a few percent of the incoming amplitude for small angles of incidence. For angles of incidence close to 90°, however, the relative amplitude approaches 100%. In the case of total internal reflection, the incoming ray is reflected 100% over a range of angles and emerges with elliptical polarization (Fig. 11). We shall show that the rays impinging on the edge surface at glancing incidence contribute the most to the phenomenon of edge birefringence.

One might wonder about the applicability of Fresnel's equations which are commonly used in situations where a wide beam (wide compared with the wavelength λ of light) illuminates an extended dielectric interface. However, the edge surfaces of thin crystal flakes examined by us are only between $\lambda/3$ and 2λ thick. Also, our model calculation does not take into account diffraction phenomena, which ought to contribute to image details that are close to the resolution limit of the microscope. Let us first present the results of our model calculation whose success is part of the answer to the above questions. We will give a more detailed account later in the discussion.

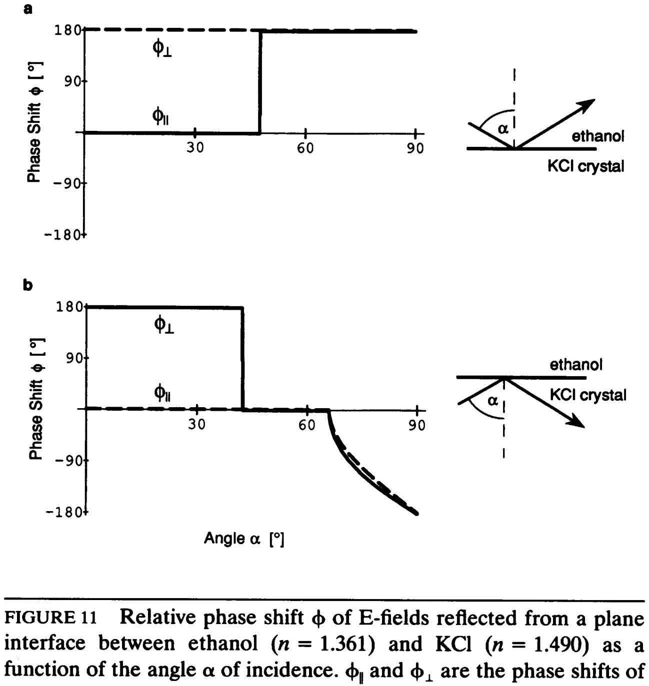

FIGURE 11 Relative phase shift ϕ of E-fields reflected from a plane interface between ethanol (n = 1.361) and KCl (n = 1.490) as a function of the angle α of incidence. $\phi_{\parallel}$ and $\phi_{\perp}$ are the phase shifts of the components polarized parallel and perpendicular to the plane of incidence. (*a*) Light ray incident from the solvent side; (*b*) from the crystal side. In *b* the ray is totally internally reflected and emerges as elliptically polarized light for angles α larger than 66°. In *a* the Brewster angle is 47.5°, in *b* it is 42.4° (at the Brewster angle, the amplitude of the reflected field component polarized parallel to the plane of incidence is zero).

In our model calculation, a light ray was represented by a list of ray parameters which included a point through which the ray passed, the direction in which it propagated, and the complex amplitude of the E-field. During the calculation, the ray parameters were modified successively by functions representing optical elements or devices. As detailed below, the ray parameters were passed from one function to the next, similar to a light ray passing from one device to the next on an optical bench.

Procedure

We have calculated image intensities of a thin KCl crystal flake using the "optical set up" shown in Fig. 12. In this figure three rays are depicted representing three categories of rays which make important contributions to the intensity at a given image point. The rays are distinct through their interaction with the crystal edge and their mutual phase relationships: Ray 1 is transmitted through the crystal edge. Ray 2 is reflected by the crystal edge. Ray 3 is a direct ray which does not hit the cystal edge, but it is coherent to the reflected ray. Rays 2 and 3 are mutually coherent because they come from the same point in the back focal plane of the condenser. For each reflected ray there is one coherent direct ray which arrives at the same image point. In general, the reflected ray 2 has a longer path length than the direct ray 3 (Fig. 13). This difference in path length was taken into account in the calculation of the mutual phase relationship between rays 2 and 3. Most rays which arrive at an image point near the edge belong to one of the three categories of rays, 1, 2, and 3. There is still a fourth category of rays, namely the rays which do not hit the crystal edge and are incoherent to all other rays (incoherent direct rays).

In Fig. 14 we show the distribution of the four categories of rays in the back focal plane of the objective lens for two image points near the crystal edge. The back focal plane of the objective was divided into a two-dimensional grid pattern. The grid pattern served as a guide to select a representative number of rays arriving at a given image point. The paths of the rays from the image point through the center of each grid element were calculated by ray tracing. The ray paths were first established starting from the image point through the objective lens to the crystal and beyond to the back focal plane of the condenser. At the back focal plane of the condenser the ray direction was inverted and an initial electric field vector representing the light field was added to the ray parameters.

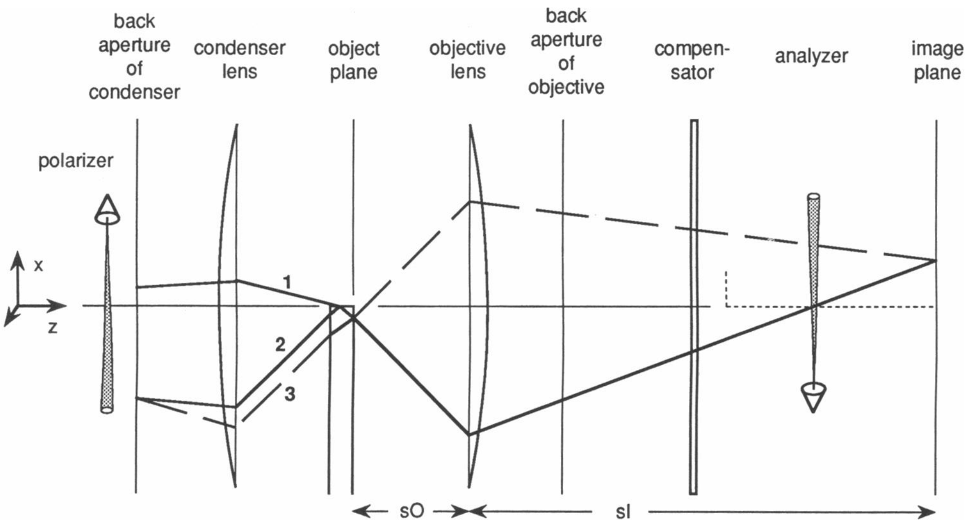

FIGURE 12 Cross-section through the optical setup used for the model calculation. Light propagates from left to right. The left lens corresponds to the condenser and the right lens to the objective of a light microscope. Both were assumed to be thin lenses with the same focal length. Between the lenses, a thin crystal plate is placed with its edge near the axis of the lenses. The narrow edge surface extends horizontally. The condenser and objective are set symmetrically with respect to the crystal front surface. Other optical elements include a polarizer, a thin birefringent crystal as compensator and an analyzer. Three ray paths are shown that arrive at the same image point near the edge inside the crystal (see text). For clarity in the drawing the object distance sO and the image distance sI were chosen such that the front surface of the crystal is imaged by the objective with the lateral magnification factor of 4. The dotted lines indicate the axial extension of the crystal image formed by the objective (the axial magnification is the square of the lateral magnification).

Along the path from the back focal plane of the condenser to the image point, the electric field vector was modified successively by the optical elements passed. The following is a description of the functions representing the different optical elements which are listed in the same sequence as they were passed by the ray:

Polarizer: The transmission direction of the polarizer was parallel to the $\{1, -1, 0\}$ direction and the electric field amplitude of each ray was set to 1. The ray path was not affected.

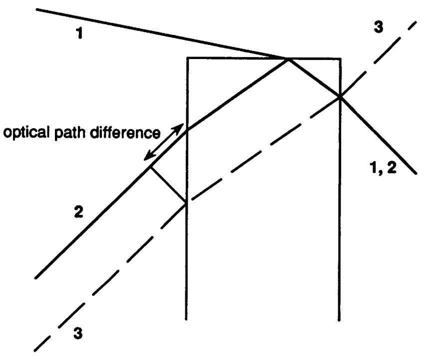

FIGURE 13 Detail of Fig. 12 showing the ray traces near the crystal edge. The difference in optical path length between ray 2 and 3 is indicated.

Condenser lens: The ray path was bent according to the thin-lens equation at a single principal plane which was normal to the optical axis (z-axis). The electric field vector of the ray was expressed in two components, the component perpendicular and parallel to the plane of incidence. The plane of incidence is defined by the normal to the principal plane and the ray direction. The field component perpendicular to the plane of incidence was left unchanged, while the component parallel to the plane of incidence was rotated by the same angle as the ray was bent.

Crystal: The crystal was defined by three surfaces: the back surface close to the condenser, the front surface close to the objective and the edge surface. The back and the front surfaces extended infinitely in one-half plane and were oriented perpendicular to the z-axis. The edge surface had a finite width in the z direction and an infinite extension in the y-direction. A given light ray hit either all three surfaces or only two or one or none, depending on its path. If it hit a surface the ray path was bent according to Snell's law. For the front and back surfaces, only the transmitted beams were entered into the calculation, while for the edge surface both the transmitted and reflected beams were entered. At each interface the field of the incoming ray was split into the components perpendicular and parallel to the plane of incidence. The amplitudes and phases of the transmitted

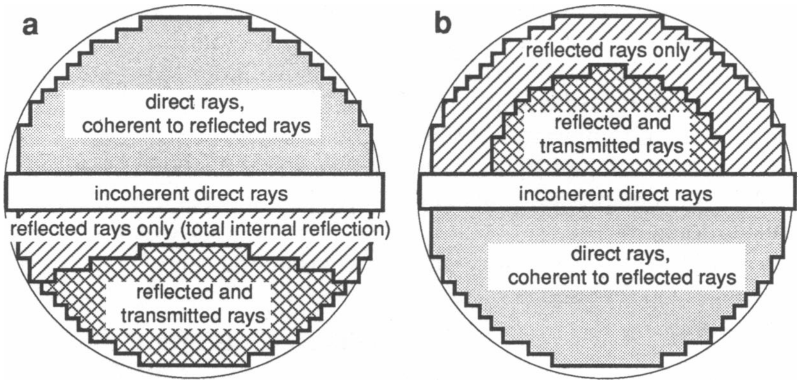

FIGURE 14 Outlines of grid patterns in back focal plane of objective lens. The outlines show the distribution of rays that were either transmitted or reflected by the crystal edge or did not interact with the edge at all. All rays arrived at a single image point near the edge either inside *a* or outside *b* the crystal (also see Fig. 12). The steps in the outlines indicate the size of the grid elements typically used for the calculation. The distributions shown were computed for a numerical aperture of 1.1, a crystal thickness of 2 λ (λ wavelength of light), a magnification factor of 100, imaging two points in the plane of the crystal front surface. The points were displaced from the edge by 0.2 λ.

and reflected E-fields were calculated with Fresnel's equations.

Objective lens: The functions representing the objective and condenser lens were identical. We assumed in the calculation that both objective and condenser did not change the state of polarization of the light ray, because we used rectified optics in our experiments. While nonrectified lenses, even those that are strain-free, rotate the polarization of a light ray somewhat, rectified optics counteract this rotation and preserve the state of polarization (Inoué and Hyde, 1957).

Compensator: The compensator simulated in the model calculation corresponded to the Brace-Köhler compensator used in our experiments. It consists of a thin, birefringent crystal plate which can be rotated around one principal axis, which is parallel to the optical axis of the setup. In the reference position with zero rotation angle, the slow axis of the compensator was oriented parallel to the $\{1, 1, 0\}$ direction (analyzer direction). In the model calculation the E-field of the ray was expressed first in terms of the components parallel to the slow and fast axis. Then a relative phase shift of λ/30 or 12° was introduced between the two components. The ray path was not affected.

Analyzer: The transmission direction of the analyzer was parallel to the $\{1, 1, 0\}$ direction (crossed position to polarizer). The E-field component perpendicular to the analyzer direction was set to zero. The ray path was not affected.

The solvent surrounding the crystal was assumed to fill the space between the principal planes of condenser and objective. The numerical apertures of the condenser and the objective were defined as usual by $n_{\text{solvent}} * \sin\Theta$, with Θ half the cone angle of either the illuminating rays from the condenser or of the rays collected by the objective. In the calculation the numerical apertures were set by the radii of the stops in the back focal planes of condenser and objective.

As a consequence of the high magnification factor 100 of the objective lens, the ray paths between the objective and the image plane were almost parallel to the optical axis. Hence, the z-components of the E-fields were small, with the field vectors essentially parallel to the x-y plane. Therefore, we neglected the small z-components of the E-fields for the calculation of the field changes induced by the compensator and analyzer.

The intensity at a given image point was calculated with the field values of all rays selected with the help of the grid pattern in the back aperture plane of the objective. The field values of mutually coherent rays were added and stored in memory together with the field values of all other rays. To obtain the image intensity for a particular compensator and analyzer setting, the phase retardation of the compensator and the transmission characteristic of the analyzer were applied to the field values and the resulting E-fields were squared and summed. This way, the field values for an image point were computed only once, and the intensities for all compensator and analyzer settings could be derived from this one set of field values.

In the calculation, the length scale was defined by λ, the wavelength of light in vacuum. Therefore, the lay-out of the optical setup was given in units of λ. The focal lengths of condenser and of objective lens were set to 1,000 λ. The size of one grid element in the back focal plane of the objective (see Fig. 14) was typically 50 λ. This choice of grid size led to more than 400 rays used for the computation of the intensity at a given image point, for a numerical aperature of 0.6. The 400 different field values of one image point were computed with the procedure described above in ~15 min. (The grid size was chosen small enough that further reduction did not significantly change the results of the computation.) The special ray tracing program was developed by us with Mathematica on a Macintosh IIx. The program was not optimized for speed of calculation.

In the following section we present a study of calculated intensity profiles obtained with crossed polarizers and different compensator settings.

RESULTS

Calculated intensities near crystal edge

When we compare a calculated intensity profile (Fig. 15) to an experimental one (Fig. 5), we can recognize that the main characteristics of the experimental data were reproduced by the calculation. In both, the calculated and experimental profiles one finds an intensity minimum and maximum which border the edge and which exchange positions when going from positive to negative compensator settings. The extremum on the low refractive index side is smaller in amplitude than the one on the high refractive index side. The intensities in both extrema are mostly affected by light rays which go through the central areas of the back focal planes of objective and condenser, because the low NA rays arrive at the edge surface at glancing incidence and are reflected with high efficiency. The low NA rays, if they arrive from the high refractive index side, are totally internally reflected by the edge surface and become elliptically polarized (Fig. 11 *b*). The elliptical polarization of the totally internally reflected rays on the high refractive index side leads to the strong maximum and the high apparent birefringence which we also observed in our experiments.

In the calculated patterns of Fig. 15, the mutual distance between the maxima nearest to the edge is 0.5 $\lambda = 0.27$ µm, which is somewhat smaller than the experimental value (see Fig. 5).

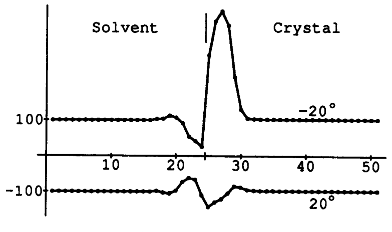

FIGURE 15 Calculated intensity profiles across a crystal edge. Profiles were computed at different compensator settings shown on the right of the graph. The profiles with negative intensity values were displaced for clarity by subtracting a constant from the original data. The solvent ethanol is to the left, the KCl crystal to the right of the top vertical line which indicates the position of the edge. The crystal thickness was set to twice the wavelength, objective and condenser NA were 0.6, intensities were scaled with an arbitrary scaling factor. The calculated intensities should be compared with the experimental data in Fig. 5.

Calculated intensities versus compensator angles

The calculated intensities near the edge (Fig. 16) vary with the compensator setting in a similar fashion as the experimental data (Fig. 6). The displacements of the minima at the solvent side and the crystal side, as shown in Fig. 16, lead to retardance values of −3.3 and 5.8 nm, respectively. This is about a factor 1.5 larger than the corresponding experimental values.

Calculated retardances versus solvent refractive index

The calculated retardances decrease linearly with the difference in refractive index of solvent and crystal (Fig. 17). This theoretical result corresponds to our experimental finding summarized in Fig. 9.

Calculated retardances versus crystal thickness

The retardance near the crystal edge decreases linearly with decreasing crystal thickness. The thinner the crystal, the fewer rays will hit the edge surface. Fig. 18 demonstrates the close to linear relationship between

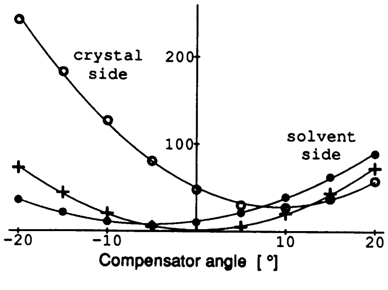

FIGURE 16 Calculated intensities in extrema near crystal edge versus compensator setting. Filled circles are intensities calculated for the solvent side, open circles for the crystal side, crosses represent the background intensities. Continuous lines are parabolic fits to the data points. Intensities were calculated with the same parameters as described in the legend to Fig. 15. The calculated intensities should be compared with the experimental data in Fig. 6.

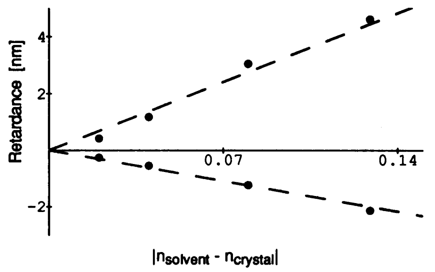

FIGURE 17 Calculated retardances near the crystal edge versus the difference in refractive index between the solvent and the crystal (crystal thickness 1 λ = 0.546 μm). Positive retardances were calculated at the high refractive index side, negative retardances at the low refractive index side of the crystal edge. The dashed lines are linear fits through the points.

the percentage of rays interacting with the edge versus the height of the edge surface. The percentage of all rays being transmitted or reflected by the edge surface is also called the total cross-section of interaction. The linear relationship between the calculated total cross-section and the height of the edge surface corresponds to our experimental finding on the measured retardance versus crystal thickness, summarized in Fig. 10. In contrast to the total cross-section, however, the calculated retardance of each image point did not vary with the height of the edge surface in the same linear fashion. Especially for image points very close to the edge (e.g., distance 0.02 λ), the calculated retardance decreased only by very little (<25%, instead of 84%) when the height of the edge surface was decreased from 2 λ to 0.33 λ. For an image point very close to the edge, the specific cross-section, i.e., the percentage of rays arriving at that image point and having interacted with the edge, is almost independent of the height of the edge surface. At this point, pure ray tracing has led to misleading results which are probably corrected by taking into account the diffraction phenomena which limit the resolution of the image. We will comment on this in more detail in the upcoming discussion.

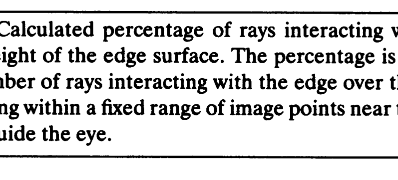

FIGURE 18 Calculated percentage of rays interacting with the edge versus the height of the edge surface. The percentage is calculated as the total number of rays interacting with the edge over the number of all rays arriving within a fixed range of image points near the edge. The lines are to guide the eye.

DISCUSSION

We have demonstrated good agreement between measurement and theory regarding edge birefringence, with respect to its sign, distribution across the edge, relative magnitudes of the maxima on the higher and lower refractive index sides, and dependence on refractive indices of material on the two sides of the boundary. It was also noted that edge birefringence arises regardless of the phase of the materials (solid, liquid, or gas) making up the two sides of the boundary. These observations argue strongly that edge birefringence is a physical optical phenomenon that is attributable to the presence of the optical boundary itself.

Naturally, for some specimens, anisotropically oriented, or structured, material is also present at the interface and would be expected to contribute to birefringence in that region. Nevertheless, the contribution of edge birefringence must first be accounted for before the birefringence due to anisotropy of those material can be established.

In our theoretical analysis, it is somewhat surprising that ray tracing and Fresnel's equations, both commonly considered macroscopic attributes of ray behavior at interfaces, should predict edge birefringence, a microscopic optical phenomenon, as well as in fact they do. In the case of edge birefringence of thin crystal flakes, the dielectric interface in question is elongated in one dimension only, whereas the other dimension is of the order of the wavelength of light. This reduction in one dimension seems to preserve the main characteristics of the scattering of light by the interface as it is described by Fresnel's equations.

However, our theory is still an approximation, and does not completely predict the quantitative details of edge birefringence. In particular, the calculated magnitudes of the principal maxima and minima are larger than the measurements by a factor of 1.5, sharp inflections absent in the observations appear in the calculated distribution of birefringence, and the theory does only indirectly predict the dependence of the magnitude of edge birefringence on the thickness of the specimen. A refinement in the calculation that takes into account diffraction phenomena should provide a better quantitative prediction.

A different avenue in explaining edge birefringence was taken by Takenaka and Rikukawa (1974), who formulated a microscopic theory based on the anisotropy of the local electric fields polarizing the atoms near the interface. Considering the difficulty of defining the local electric field even in bulk materials (Landauer, 1978), it seems problematic to base the calculation of edge birefringence on this somewhat ill-defined concept. Furthermore, in constructing the theory, assumptions were made about the crystalline structure and the mutual interactions of the atoms near the interface. These specific assumptions seem to be at odd with the general nature of edge birefringence which is observed near dielectric interfaces of all kinds, such as gas-liquid, gas-solid, solid-solid, etc. Nevertheless, the theory does seem to account for the change in sign of the birefringences observed on either side of the edge. However, the theory of Takenaka and Rikukawa makes no clear predictions on the magnitude of edge birefringence, e.g., how it varies with sample thickness. The one numerical example demonstrated starts with very specific crystal data of NaCl and then neglects the influence of the outside material. Because the conditions of the numerical example and of the experimental observations remain unclear, we feel unable to compare the results of Takenaka and Rikukawa with our experimental and theoretical findings. Our phenomenological theory is based on observable parameters, such as the refractive index, and experimentally well-defined concepts such as ray tracing and Fresnel's equations. Naturally, our theory is not complete and we believe that a rigorous treatment of edge birefringence observed near edges of small objects can only be achieved through scattering theory. For larger objects then, with straight faces, we expect that the results of the scattering theory will approach the results derived with Fresnel's equations and ray tracing as we report them here.

Diffraction phenomena tend to limit the resolution of the image averaging the image intensities of object points that have a mutual distance smaller than approximately half a wavelength. To include this effect we have averaged the calculated image intensities over a range of several neighboring image points. The smoother shape of the resulting intensity profiles were considerably closer to the measured profiles. Interestingly enough, the birefringences calculated after averaging the intensities predicted the linear decrease in edge birefringence with crystal thickness, as it is observed in our experiments.

We also observed, especially at low condenser NA, additional maxima of retardance farther away from the edge (see Fig. 8). This observation is not predicted by our model calculation. Based on our experimental observations we speculate that the additional maxima are a consequence of the diffraction of especially those rays which propagate almost parallel to the edge surface.

Our model calculations do show, as observed in our measurements, that the distances between the specimen boundary and the maxima and minima of edge birefringence are less than the distance between the maximum and the first minimum of a standard diffraction pattern produced by the same lenses. In other words, it appears that edge birefringence can provide a means to define the location of, and measure the distances between, edges more precisely than with determinations made by other methods of microscopy that generate contrast at sharp optical boundaries. For example, contrast of the image is also reversed at, or near edges, in differential interference contrast (DIC, or Nomarski) microscopy. However, the spatial distribution of the maxima and minima with DIC optics is not a sole function of the step in refractive index. Instead, it depends on whether the refractive index rises or falls along the shear direction of the Wollaston or Nomarski prisms. With edge birefringence, the maxima and minima appear symmetrically with respect to the step rise and fall of the refractive index, so that the ambiguity of the location of the edge seen in DIC should not be present.

Thus, in addition to explaining the birefringence that is inherent at all refactive index boundaries (i.e., whereever, the dry mass of the specimen changes abruptly), edge birefringence can pinpoint the exact location of such boundaries. In a separate paper we will report on the images of muscle fibrils observed with high extinction polarized light microscopy and present our analysis on the distribution of anisotropy and dry mass of material along the length of the sarcomere.

CONCLUSION

We conclude from our experimental and theoretical study, that edge birefringence is a general optical phenomenon that appears near boundaries of objects, small or large, that have a different refractive index than the surrounding medium. Edge birefringence is a consequence of the optical boundary itself, and not of the structural details in the vicinity of the boundary. Our analysis, however, is by no means complete, theoretically as well as experimentally, for we have not studied quantitatively the change in observed retardance, e.g., with focus position, with tilt angle of the interface, or with the steepness of the refractive index gradient at the interface. Diffraction phenomena have to be taken into account for a more faithful reproduction of image details. Therefore, further studies are necessary to make edge birefringence useful in measuring the three-dimensional distribution of dielectric interfaces in the specimen. Our present article, however, has demonstrated that by taking advantage of computer-assisted image analysis and theoretical modeling, edge birefringence is accessible to a quantitative analysis and prom-

ises to be an important tool in the eternal quest for the discovery of ever finer structural details in the living cell and elsewhere.

The author dedicates this article to Dr. Shinya Inoué, distinguished scientist at the Marine Biological Laboratory, on the occasion of his 70th birthday. The analysis presented here is a first quantitative account of edge birefringence which Shinya Inoué first recognized as an optical phenomenon some 30 years ago (Inoué, 1959). Since then, he challenged many prominent researchers in optics and optical microscopy to tackle this problem and to give a quantitative, clear, and intelligible account of this important optical phenomenon (Inoué, 1988). After it remained elusive for so many years, he finally found someone, familiar with birefringence, educated in optical physics, willing to give whatever it takes to reach this goal. I am very grateful to Shinya Inoué for proposing the project, for critique of the manuscript, and for continued support including use of his laboratory and equipment throughout the project. I hope that the result can measure up to the high standards found in the content and presentation of Inoué's own research work.

The author also thanks the collaboration of Louis Kerr of the M.B.L. who was responsible for the scanning electron microscopy. These studies were supported in parts by National Institutes of Health grant R-37 GM31617 and National Science Foundation grant DCB-8908169 awarded to Dr. Inoué.

Received for publication 21 January 1991 and in final form 21 May 1991.

REFERENCES

Ambronn, H., and A. Fray. 1926. Das Polarisationsmikroskop, seine Anwendung in der Kolloidforschung in der Färberei. Akademischer Verlag, Leipzig.

Barer, R. 1959. Phase, interference and polarizing microscopy. *In* Analytical Cytology. 2nd edition. R. C. Mellors, editor. McGraw-Hill, New York. 169–272.

Block, S. M., K. A. Fahrner, and H. C. Berg, 1991. Visualization of bacterial flagella by video-enhanced light microscopy. *J. Bacteriol.* 173:933–936.

Hartshorne, N. H., and A. Stuart. 1960. Crystals and the polarizing microscope: a handbook for chemists and others. 3rd edition. Arnold, London.

Hecht, E. 1987. Optics. Addison- Wesley Publ. Co., Reading, MA.

Inoué, S. 1953. Polarization optical studies of the mitotic spindle. I. The demonstration of spindle fibers in living cells. *Chromosoma.* 5:487–500.

Inoué, S. 1959. Problems in polarization microscopy. *J. Opt. Soc. Am.* 49:508.

Inoué, S. 1986. Video Microscopy. Plenum Press, New York.

Inoué, S. 1988. High extinction, high sensitivity polarization microscopy. *In* Analytical and Quantitative Light Microscopy in Biology, Medicine and Materials Science. Videotape Edition. R. A. Knudson, Technical Video Ltd., P.O. Box 693, Woods Hole, MA 02543.

Inoué, S. 1990. Foundations of confocal scanned imaging in light microscopy. *In* Handbook of Biological Confocal Microscopy. J. B. Pawley, editor. Plenum Publ. Corp., New York. 1–14.

Inoué, S., and K. Dan. 1951. Birefringence of the dividing cell. *J. Morphol.* 89:423–456.

Inoué, S., and W. L. Hyde. 1957. Studies on depolarization of light at microscope lens surfaces. II. The simultaneous realization of high resolution and high sensitivity with the polarizing microscope. *J. Biophys. Biochem. Cytol.* 3:831–838.

Inoué, S., and H. Kubota. 1958. Diffraction anomaly in polarizing microscopes. *Nature (Lond.).* 182:1725–1726.

Inoué, S., and H. Sato. 1966. Deoxyribonucleic acid arrangements in living sperm. *In* Molecular architecture in cell physiology. T. Hayashi and A. G. Szent-Gyorgyi, editor. Prentice-Hall, Englewood Cliffs, NJ. 209–248.

Inoué, S., and A. G. Szent-Gyorgyi. 1958. Only major public presentation of birefringence patterns of muscle fibrils at high resolution. The fine details of the patterns were mistaken to reflect the distribution of the structure proteins. 2nd Annual Meeting of the Biophysical Society, Cambridge, MA.

Keller, H. E. 1990. Objective lenses for confocal microscopy. *In* Handbook of Biological Confocal Microscopy. J. B. Pawley, editor. Plenum Publ. Corp., New York. 77–86.

Landauer, R. 1978. Electrical conductivity in inhomogenous media. *In* Electrical transport and optical properties of inhomogeneous media. J. C. Garland, and D. B. Tanner, editors. AIP Conference Proceedings, New York. 40:2–45.

Lutz, D. A., and S. Inoué. 1986. Techniques for observing living gametes and embryos. *In* Methods in Cell Biology. L. Wilson, editor. Academic Press, New York. 89–110.

Schmidt, W. J. 1924. Die Bausteine des Tierkörpers in polarisiertem Lichte. Cohen, Bonn.

Schmidt, W. J. 1937. Die Doppelbrechung von Karyoplasma, Zytoplasma und Metaplasma. Bornträger, Berlin.

Takenaka, H., and K. Rikukawa. 1974. Rectified optics and edge birefringence. *Jap. J. Appl. Phys.* 14:429–433.

Walker, R. A., S. Inoué, and E. D. Salmon. 1989. Asymmetric behavior of severed microtubule ends after ultraviolet-microbeam irradiation of individual microtubules in vitro. *J. Cell Biol.* 108:931–937.

Wright, F. E. 1911. The methods of petrographic–microscopic research: their relative accuracy and range of application. Carnegie Institution of Washington, Washington, D.C.